Critical phenomenon of the ferromagnet Cr_2Te_3 with strong perpendicular magnetic anisotropy

Aina Wang,[1,2] Zan Du,[1,2] Fanying Meng,[1,2] Azizur Rahman,[2] Wei Liu,[3] Jiyu Fan,[4] Chunlan Ma,[5] Langsheng Ling,[1,6] Chuanying Xi,[1,6] Min Ge,[7] Li Pi,[1,6,7] Yuheng Zhang,[1,6,7] and Lei Zhang[1,6,*]

[1] *Anhui Key Laboratory of Low-Energy Quantum Materials and Devices, High Magnetic Field Laboratory, Hefei Institutes of Physical Science, Chinese Academy of Sciences, Hefei 230031, China*

[2] *University of Science and Technology of China, Hefei 230026, China*

[3] *Institutes of Physical Science and Information Technology, Anhui University, Hefei 230601, China*

[4] *Department of Applied Physics, Nanjing University of Aeronautics and Astronautics, Nanjing 210016, China*

[5] *Jiangsu Key Laboratory of Micro and Nano Heat Fluid Flow Technology and Energy Application, School of Physical Science and Technology, Suzhou University of Science and Technology, Suzhou 215009, China*

[6] *The High Magnetic Field Laboratory of Anhui Province, Hefei 230031, China*

[7] *Hefei National Research Center for Physical Sciences at Microscale, University of Science and Technology of China, Hefei 230026, China*

(Received 22 April 2024; revised 19 July 2024; accepted 7 August 2024; published 4 September 2024)

Chromium telluride Cr_xTe_y has great potential applications in spintronics due to its intrinsic ferromagnetism and strong magnetic anisotropy. In this study, we systematically investigate magnetic properties of a ferromagnetic Cr_2Te_3 single crystal with strong perpendicular magnetic anisotropy (PMA). Apart from ferromagnetic-to-paramagnetic (FM-PM) transitions at $T_C \sim 181$ K for both $H//c$ and $H//ab$, other exotic magnetic behaviors are revealed, such as a field-modulated first-order transition uncovered by the anisotropic magnetization, a canted FM coupling rather than previously reported spin-glass behavior demonstrated by the ac susceptibility. Furthermore, anisotropic magnetization reveals significant PMA stronger than any other Cr-based transition metal chalcogenide, with a negligible saturation field for $H//c$ but a distinct one up to 155 kOe for $H//ab$. Critical exponents $\beta = 0.340(5)$, $\gamma = 1.114(1)$, and $\delta = 4.504(5)$ are obtained for $H//c$, which fall between the three-dimensional (3D)-XY and 3D-Ising models indicative of anisotropic magnetic coupling. An H-T phase diagram of the Cr_2Te_3 single crystal is constructed for $H//c$, which distinguishes canted FM1, canted FM2, forced FM (FFM), and PM phases. The phase diagram indicates that the transition to the canted FM2 under lower fields is of a first-order type, which is suppressed into a second-order one by the external magnetic field. The multiple phase transitions and complex magnetic structures is suggested to derive from the competition between the intralayered superexchange (FM couplings) and the interlayered direct interaction (AFM coupling). The various magnetic configurations and strong PMA make Cr_2Te_3 highly promising for spintronic device applications.

DOI: 10.1103/PhysRevApplied.22.034006

I. INTRODUCTION

Exploration of two-dimensional (2D) materials with long-range magnetic ordering is crucial for the development of spintronic devices, particularly 2D ferromagnets with high Curie temperature (T_C) and strong magnetic anisotropy. Since the successful synthesis of intrinsic ferromagnetic (FM) materials such as $Cr_2Ge_2Te_6$ and CrI_3, significant attention has been given to transition metal chalcogenides (TMDCs) and transition metal halides [1,2]. Meanwhile, the chromium telluride Cr_xTe_y family is expected to have practical applications in devices such as magnetic tunneling junctions and spin-field-effect transistors due to their high T_C above room temperature [3,4]. The crystal structures of the Cr_xTe_y family, also known as $Cr_{1+\delta}Te_2$, can be treated as the insertion of different ratios of Cr atoms between $CrTe_2$ van der Waals (vdW) gaps, which are then stacked in various arrangements along the c direction to form diverse structures. These compounds are easily synthesized, highly controllable, and sensitive to Cr atoms, resulting in various properties, such as giant magnetoresistance (GMR) effects, anomalous Hall effects (AHE), and exotic topological spin textures [5–8]. For instance, Cr_5Te_8 with $T_C \sim 230$ K exhibits

*Contact author: zhanglei@hmfl.ac.cn

strong perpendicular magnetic anisotropy (PMA), robust ferromagnetism, and large AHE [6,9]. Cr_5Te_6 shows a colossal topological Hall effect maintained until 270 K due to noncoplanar spin textures [10]. Cr_3Te_4 has an unusual biskyrmion and a layer-dependent magnetic anisotropy, the easy axis of which shifts from in-plane to out-of-plane as the thickness decreases [11–13]. The van der Waals material $CrTe_2$ exhibits the same layer-dependent magnetic anisotropy behavior as Cr_3Te_4. However, the intrinsic magnetic state of its monolayer remains controversial [14,15]. $CrTe_3$ displays rare antiferromagnetic (AFM) semiconductor behavior in the Cr_xTe_y family [16]. The magnetic and electronic structures of Cr_xTe_y can be regulated through a variety of means such as magnetic field, electronic field, thickness, and pressure [15,17–19]. It has been demonstrated that Cr_xTe_y exhibits a layer-number-dependent T_C and magnetic anisotropic directions [15,17–19]. Furthermore, this system undergoes pressure-induced lattice changes, such as a structural transition from NiAs-type to MnP-type at 13 $\sim$ 14 GPa in CrTe [20], a semiconductor-to-metal transition at 24 GPa in $Cr_{1-\delta}Te$ [21], and the tuning of the ground state between ferromagnetism and antiferromagnetism by in-plane strain in $CrTe_2$ [22].

In the Cr_xTe_y family, Cr_2Te_3 stands out because of its robust ferromagnetism, which maintains in a fewer-layered sample or even in a single layer [23]. Usually, in most Cr_xTe_y compounds, the interface effect can result only in linear magnetic ordering [14,24]. However, the surface effect can induce the formation of topological magnetic structures in Cr_2Te_3, such as magnetic skyrmions in 2D-Cr_2Te_3/Cr_2Se_3 [25], Cr_2Te_3/Bi_2Te_3 [26], and Cr_2Te_3/Bi [27] heterostructures. On the other hand, Xu *et al.* successfully grew vdW $CrGeTe_3$ single crystals based on non-vdW Cr_2Te_3 [28,29]. Chi *et al.* reported an interface-tunable Berry curvature in Cr_2Te_3 [30]. The PMA and spin-glass-like behavior in Cr_2Te_3 thin films have also been studied. All these efforts and findings make Cr_2Te_3 a promising candidate for electronic device applications.

However, for Cr_2Te_3, there are debates surrounding the spin-glass-like behavior and the disregard for in-plane magnetism. In this work, we aim to systematically investigate the magnetic anisotropy and couplings of Cr_2Te_3 single crystals. The study of magnetization reveals exotic magnetic behaviors in addition to FM-PM transitions for $H//c$ and $H//ab$, such as a field-modulated first-order transition, a canted FM coupling rather than previously reported spin-glass behavior, a significant PMA with a negligible saturation field for $H//c$ but a distinct one for $H//ab$. The critical exponents obtained for $H//c$ fall between the three-dimensional (3D)-*XY* and 3D-Ising models, indicating the presence of anisotropic magnetic coupling. An H-T phase diagram for Cr_2Te_3 single crystal is constructed for $H//c$, clarifying the canted FM1, canted FM2, forced FM (FFM), and PM phases. The phase diagram reveals that the transition to the canted FM2 under lower field is of a first-order type, while that from the canted FM2 or FFM to PM under higher field is of a second-order one. This indicates that the first-order magnetic transition can be suppressed into a second-order one by the external magnetic field. The multiple phase transitions and complex magnetic structures are suggested to arise from the superexchange within the *a*-*b* plane and the direct interaction along the *c* axis.

II. EXPERIMENTAL METHODS

Single crystals of Cr_2Te_3 were synthesized using a chemical vapor transport (CVT) method with I_2 serving as the transport agent [31]. High-purity powders of Cr (99.99%, Alfa Aesar) and Te (99.99%, Alfa Aesar) were mixed thoroughly with the stoichiometric ratio in an Ar-glove box and sealed into an evacuated quartz tube. The quartz tube was heated to 1000 °C on the source zone and 750 °C on the other side. After holding for 7 days, the tube was cooled to room temperature, and the single crystals were acquired on the cold side. The crystalline structure was characterized by x-ray diffraction (XRD) with Cu Kα radiation using a Rigaku-TTR3 diffractometer. The powder was ground from the single crystals to carry out the powder XRD pattern. To further analyze the crystals, high-angle annular dark-field scanning transmission electron microscope (HAADF-STEM) and energy dispersive x-ray (EDX) spectroscopy measurements were performed on a Themis *Z* double-spherical aberration-corrected transmission electron microscope operating at 300 kV. The magnetic properties were measured using a superconductive quantum interference device vibrating sample magnetometer (SQUID VSM) (MPMS-3, Quantum Design). For the initial isothermal magnetization, the sample was heated above T_C and held for 2 min. It was then cooled to the desired temperature under zero field for the isothermal magnetization measurement. The magnetization under high magnetic field up to 30 T was performed using a water-cooling resistive magnet.

III. RESULTS AND DISCUSSION

The hexagonal structural Cr_2Te_3 belongs to the space group $P\bar{3}1c$ (No. 163), as shown in Fig. 1(a) [29,32]. The unit cell consists of three types of Cr atoms, each surrounded by six Te atoms to form a coangular octahedron [23]. In the *a*-*b* plane, the Cr2 and Cr3 are tightly arranged to create a fully occupied layer, while the Cr1 atoms and numerous vacancies are alternately inserted between each of the two full layers [33]. Figure 1(b) shows the picture of the as-grown sample with a typical size of 2 × 2 mm^2, exhibiting a hexagonal sheet with a bright surface. Figure 1(c) depicts the powder (top) and single-crystal (bottom) XRD patterns. The powder XRD pattern matches the standard PDF card (29-458). The single-crystal XRD

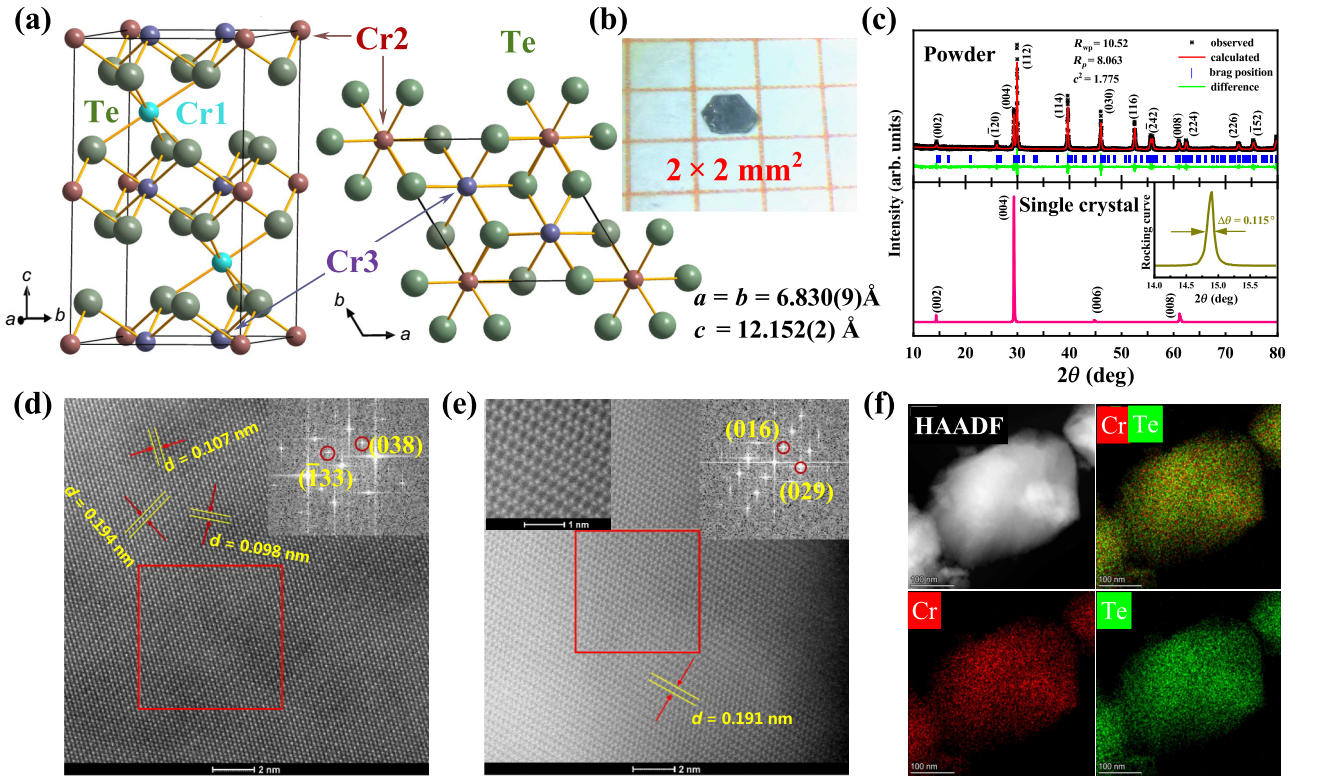

FIG. 1. (a) Crystal structure of Cr_2Te_3 from the side (left) and top (right) views. (b) Photograph of the as-grown single crystal. (c) XRD patterns for powders (top) and single crystal (bottom) along with the rocking curve in the inset. (d),(e) Atomic resolution HAADF-STEM images for two different cross sections. The right insets in (d),(e) show the corresponding FFT diagrams in red rectangular areas. (f) Elemental mapping of Cr_2Te_3 using HAADF-EDX spectroscopy.

pattern presents a set of peaks belonging to (00l), indicating that the surface of the single crystal is the a-b plane while the normal direction is along the c axis. The Rietveld refinement of the powder XRD pattern gives the lattice constants $a = b = 6.830(9)$ Å and $c = 12.152(2)$ Å, which are in agreement with previous reports [26,34]. The inset of Fig. 1(c) gives the rocking curve of the single crystal, showing a single peak with a narrow full width at half maxima ($\Delta\theta = 0.115°$). HAADF-STEM images in two different orientations are displayed in Figs. 1(d) and 1(e) to characterize the atom configurations. The honeycomb indicates the in-plane hexagonal symmetry [30]. As depicted in Fig. 1(f), the chemical compositions are estimated using transmission electron microscopy energy-dispersive x-ray (TEM-EDX) spectroscopy, which determines the stoichiometric ratio of Cr to Te is approximately 2 : 3.04. All the characterizations, including the XRD, HAADF-STEM, and TEM-EDX, demonstrate the high quality of the as-grown Cr_2Te_3 single crystals.

Due to the presence of various magnetic ions and multiple interactions involving Cr1, Cr2, and Cr3, Cr_2Te_3 demonstrates complex magnetic behaviors. Figures 2(a) and 2(b) illustrate the temperature-dependent dc susceptibility $[\chi(T)]$ and reciprocal $[\chi^{-1}(T)]$ curves with an applied field of $H = 500$ Oe along the out-of-plane ($H//c$) and in-plane ($H//ab$) orientations, respectively. The $\chi(T)$ curves were measured under three sequences: zero-field cooling measured on warming (ZFC warming),

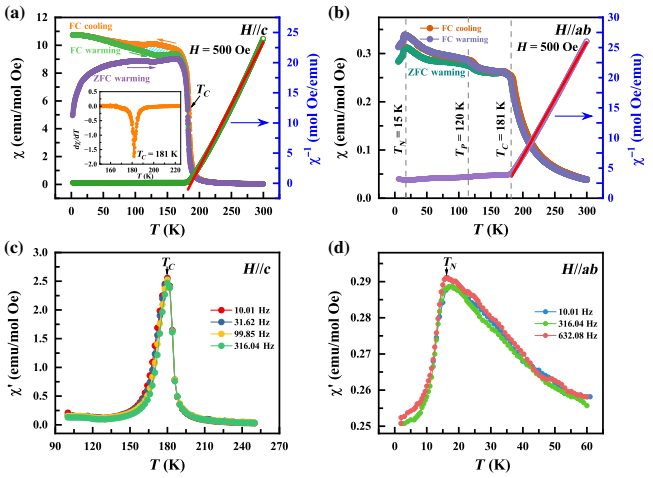

FIG. 2. Temperature dependence of dc susceptibility $[\chi(T)]$ and reciprocal $[\chi^{-1}(T)]$ with $H = 500$ Oe for (a) $H//c$ and (b) $H//ab$. Temperature-dependent ac susceptibility at different frequencies with a dc magnetic field of $H = 5$ Oe for (c) $H//c$ and (d) $H//ab$.

field cooling measured on cooling (FC cooling), and field cooling measured on warming (FC warming). In Fig. 2(a), for $H//c$, there is a sharp increase in $\chi(T)$ as the temperature decreases, indicating a paramagnetic-to-ferromagnetic (PM-FM) transition. The Curie temperature is estimated to be $T_C \sim 181$ K from the $d\chi/dT$, as shown in the inset of Fig. 2(a). Below T_C, there is a bifurcation observed in the ZFC and FC curves, which may be attributed to the coexistence of ferromagnetism and antiferromagnetism (FM and AFM) or spin-glass behaviors. Of note, a thermal hysteresis is observed between the cooling and warming curves, which typically associates with a first-order phase transition. The first-order phase transition is also manifested in structure changes and thermal-expansion measurements [35]. In Fig. 2(b), for $H//ab$, a similar PM-FM transition occurs at T_C. However, the magnetization magnitude is 30 times lower than that for $H//c$, indicating that the easy magnetization direction is along the c axis [30,34]. A bifurcation is also observed at low temperatures between the ZFC and FC $\chi(T)$ curves, but there is no thermal hysteresis between the cooling and warming curves. In addition to the magnetic transition at T_C, the other two magnetic transitions are detected at approximately 120 K and approximately 15 K. The transition at approximately 120 K may be attributed to the transition from the FM state to the canted spin configuration predicted by first-principles calculations [36,37]. The transition at approximately 15 K can be attributed to the shift from a canted spin alignment to a ferrimagnetic (FIM) state, as revealed by the neutron diffraction [38,39]. The $\chi(T)$ curves for $H//c$ and $H//ab$ exhibit distinct transitions and behaviors, suggesting strong anisotropy. The obtained T_C and magnetic behaviors are consistent with previous reports, confirming that the crystal is a good NiAs-type Cr_2Te_3 [18,25,30,34,40]. Above T_C, both $\chi(T)$ curves for $H//c$ and $H//ab$ can be fitted using the Curie-Weiss law:

$$\chi(T) = \frac{C}{T - \theta_{\mathrm{CW}}}, \tag{1}$$

where C represents the Curie constant and θ_{CW} is the Curie-Weiss temperature. The $\chi^{-1}(T)$ fittings for $H//c$ and $H//ab$ are shown on the right coordinates in Figs. 2(a) and 2(b), respectively. The effective magnetic moments are $\mu^{c}_{\mathrm{eff}} = 2.32\mu_B$/f.u. for $H//c$ and $\mu^{ab}_{\mathrm{eff}} = 2.84\mu_B$/f.u. for $H//ab$. These values are close to those reported previously, but slightly lower than the theoretical value of $\mu_{\mathrm{eff}} = 3.85\ \mu_B$ for the spin-only Cr^{3+} ion, which imply that some spins are organized in canted directions to cancel out the spin moments partially [37,38,41]. The positive values of $\theta^{c}_{\mathrm{CW}} = 194.2$ K and $\theta^{ab}_{\mathrm{CW}} = 167.1$ K indicate the presence of FM couplings in both directions.

This divergent behavior in $\chi(T)$ curves is commonly observed in the Cr_xTe_y family, which can be attributed to the presence of spin-glass or FM and AFM coexistence [9,28,40,42–45]. Roy *et al.* suggested the presence of a spin-glass behavior near 35 K by investigating the electrical resistivity of Cr_2Te_3 thin film [28]. However, Li *et al.* investigated the decaying magnetic remanence moments and demonstrated that the coexistence of FM and AFM is responsible for this behavior in $\chi(T)$ curves [40,46]. To confirm the spin configurations, the temperature-dependent ac susceptibility $[\chi'(T)]$ was measured using an oscillated ac field of 5 Oe for $H//c$ and $H//ab$, as shown in Figs. 2(c) and 2(d). A sharp peak is observed at approximately 180 K for $H//c$, while a broad peak is detected at approximately 20 K for $H//ab$. All the peaks are temperature independent, indicating that the phases in the low-temperature region are a combination of AFM and FM coexistence or canted FM, rather than a spin-glass behavior [9,47,48].

Figures 3(a) and 3(b) display the field-dependent magnetization $[M(H)]$ for $H//c$ and $H//ab$. In Fig. 3(a), the $M(H)$ below T_C increases rapidly until it reaches the saturation magnetization for $H//c$. Figure 3(c) shows the enlarged $M(H)$ at $T = 2$ K for $H//c$, revealing a small magnetic hysteresis below the saturation field of $H_S \sim 3.5$ kOe. In Fig. 3(b), the $M(H)$ for $H//ab$ increases slowly below T_C, but does not reach saturation. Both the $M(H)$ curves for $H//c$ and $H//ab$ exhibit PM behavior above T_C. For a detailed investigation of the magnetization behavior, Fig. 3(d) presents $M(H)$ for $H//ab$ up to 300 kOe (30 T). As can be seen, the $M(H)$ for $H//ab$ reaches saturation at a field of approximately 155 kOe (15.5 T) at 2 K. However, the saturation magnetization for $H//ab$ is still smaller than that for $H//c$. As the temperature increases,

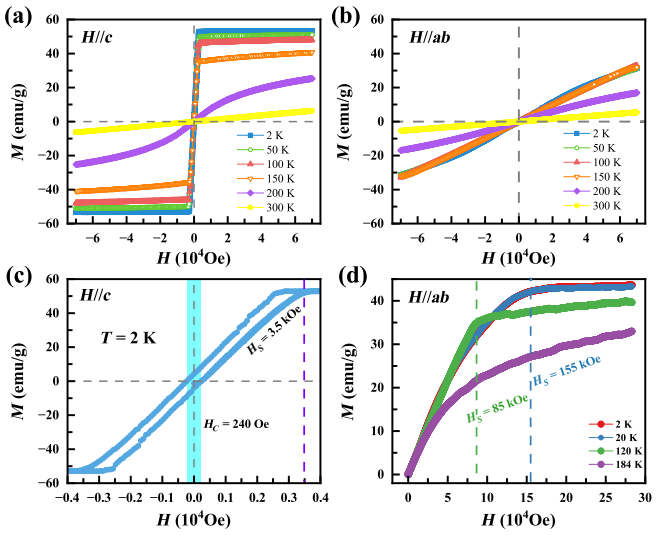

FIG. 3. (a),(b) Field-dependent magnetization $[M(H)]$ at different temperatures for $H//c$ and $H//ab$. (c) The magnetic hysteresis loop at $T = 2$ K for $H//c$. (d) Isothermal $M(H)$ curves up to high magnetic field for $H//ab$.

the saturation field decreases to 85 kOe (8.5 T) at 120 K. The ratio of H_S^{ab}/H_S^c (approximately 44.3) in Cr_2Te_3 is larger than any other Cr-based TMDCs, such as $Cr_2Si_2Te_6$ (16 times at 2 K) [49], $Cr_2Ge_2Te_6$ (2 times at 10 K) [50], and CrI_3 (1 times at 2 K) [51]. This indicates significant PMA with the easy axis along the c axis in Cr_2Te_3. The strong PMA in 2D Cr_2Te_3 is suggested to suppress thermal fluctuations, resulting in Ising-like magnetic order even in low-dimensional samples. Furthermore, strong PMA can enable intriguing topological physics, making 2D Cr_2Te_3 a promising candidate for spintronic devices [30,34].

Due to the significantly strong PMA observed in Cr_2Te_3 single crystals, it is useful to perform an in-depth study of the transition and critical behavior along the c axis. The initial isothermal $M(H)$ curves are shown in Fig. 4(a) to analyze the critical phenomenon. In general, the Arrott plot, represented by the equation $(H/M) = A + BM^2$, is a valid method for investigating the critical behaviors, which is associated with the mean-field theory with critical exponents $\beta = 0.5$, $\gamma = 1.0$, and $\delta = 3.0$. In an Arrott plot, M^2 vs H/M should result in a set of parallel straight lines in the high-field region, with the one at T_C intersecting the origin. Additionally, the positive or negative slopes of these lines can indicate the phase transitions is of a second-order (continuous) or a first-order (discontinuous) type [52]. Figure 4(b) shows the Arrott plot of Cr_2Te_3 for

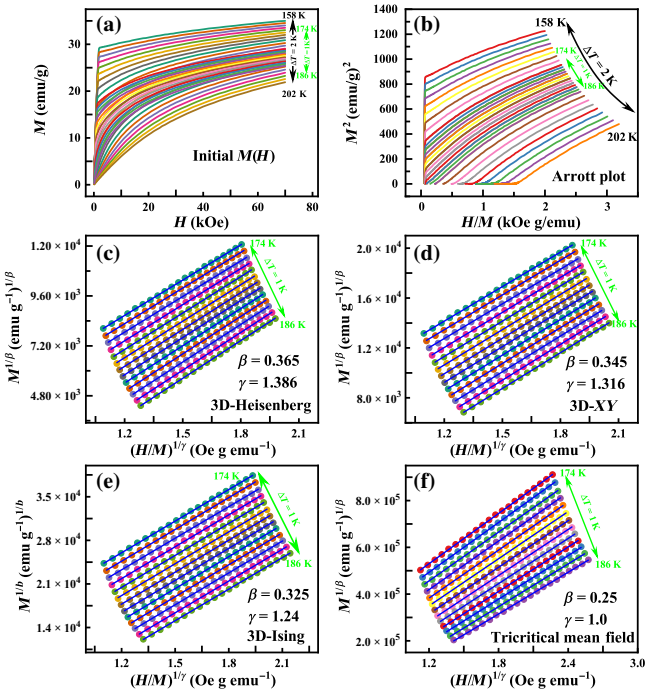

FIG. 4. (a) Initial isothermal magnetization $[M(H)]$ in the vicinity of T_C for $H//c$; (b) Arrott plots of M^2 vs H/M for $H//c$; (c)–(f) modified Arrott plots (MAPs) of $M^{1/\beta}$ vs $H/M^{1/\gamma}$ for typical theoretical models, including 3D-Heisenberg, 3D-XY, 3D-Ising, and tricritical mean-field models.

$H//c$ in the high field. The positive slopes observed in the M^2 vs H/M curves suggest that the PM-FM transition for $H//c$ is of the second-order (continuous) nature in the high field. However, these curves do not appear to be well parallel, indicating that the Arrott plot is not fully satisfied for Cr_2Te_3.

More generally, a modified Arrott plot (MAP) is utilized, which is based on the Arrott-Noakes equation of state [53]:

$$(H/M)^{1/\gamma} = (T - T_C)/T_C + (M/M_1)^{1/\beta} \tag{2}$$

where M_1 is a constant. The critical exponents β, γ, and δ correspond to the spontaneous magnetization M_S below T_C, initial magnetic susceptibility χ_0^{-1} above T_C, and critical isotherm magnetization $M(H)$ at T_C, respectively. The MAP consists of $(M)^{1/\beta}$ vs $(H/M)^{1/\gamma}$, in which these exponents fulfill the following functions [54]:

$$M_s(T) = M_0(-\varepsilon)^{\beta}, \varepsilon < 0, T < T_C \tag{3}$$

$$\chi_0(T)^{-1} = (h_0/M_0)\varepsilon^{\gamma}, \varepsilon > 0, T > T_C \tag{4}$$

$$M = DH^{1/\delta}, \varepsilon = 0, T = T_C, \tag{5}$$

where $\varepsilon = (T - T_C)/T_C$ represents the reduced temperature, h_0/M_0, M_0, and D are critical amplitudes. The MAPs are constructed using different theoretical models, including Heisenberg, Ising, XY, and tricritical mean-field models with dimensions ranging from one (1D) to three (3D). Since the three-dimensional crystal structures, only the typical MAPs for the 3D-Heisenberg, 3D-Ising, 3D-XY, and tricritical mean-field models are depicted in Figs. 4(c)–4(f), others are not shown here. All curves in MAPs exhibit quasistraight lines, although some of them such as the MAP of the tricritical mean-field model, are not parallel to each other.

To determine the best model for Cr_2Te_3, the normalized slope (NS) should be adopted, which is defined as $\mathrm{NS} = S(T)/S(T_C)$ with $S(T)$ representing the slope of single $M^{1/\beta}$ vs $(H/M)^{1/\gamma}$. The model with NS closest to "1" is considered the best for Cr_2Te_3. Figure 5(a) plots NS values for different models ranging from 1D to 3D, which indicates that 3D-Ising model is the most suitable for this system. However, the 3D-Ising model provides only the initial parameters for the iteration method. To determine the appropriate critical exponents, a rigorous iterative procedure is performed. Initially, $M_S(T)$ and $\chi_0^{-1}(T)$ are generated from MAP based on the 3D-Ising model. Then, the linear fitting to the high-field region extrapolates the intercepts of the $M^{1/\beta}$ axis and $(H/M)^{1/\gamma}$ axis. Using Eqs. (3) and (4), a set of critical parameters can be derived from $M_S(T)$ and $\chi_0^{-1}(T)$. With the obtained values of β and γ, an alternative MAP is constructed. This process is repeated until β and γ are stabilized. The final fitting of $M_S(T)$ and $\chi_0^{-1}(T)$ is shown in Fig. 5(b), in which

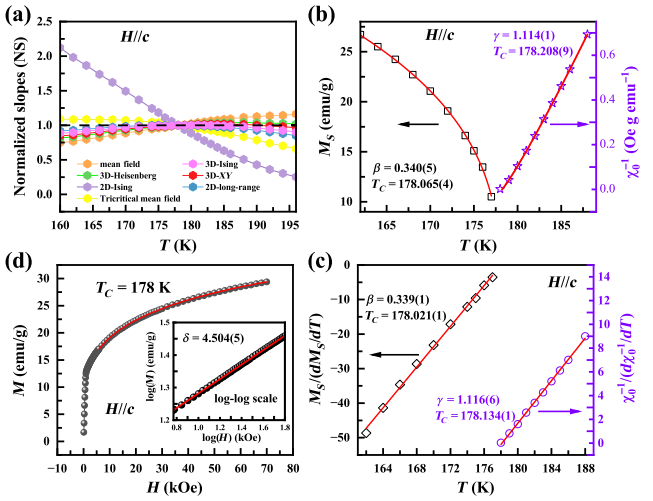

FIG. 5. Fitting results for $H//c$: (a) NS values vs T for different models; (b) M_S (left) and χ_0^{-1} (right) with the fitting curves (red); (c) KF plot for $M_S(dM_S/dT)^{-1}$ (left) and $\chi_0^{-1}(d\chi_0^{-1}/dT)^{-1}$ (right) with fitted lines; (d) fitting of initial $M(H)$ at $T_C = 178$ K with that on log-log scale in the inset.

critical exponents $\beta = 0.340(5)$ with $T_C = 178.065(4)$ K and $\gamma = 1.114(1)$ with $T_C = 178.208(9)$ K are obtained.

Alternatively, the Kouvel-Fisher (KF) technique is used to estimate the critical exponents as [55]

$$\frac{M_S(T)}{dM_S(T)/dT} = \frac{T_C - T}{\beta}, \tag{6}$$

$$\frac{\chi_0^{-1}(T)}{d\chi_0^{-1}(T)/dT} = \frac{T_C - T}{\gamma}. \tag{7}$$

The $M_S(T)/[dM_S(T)/dT]$ and $\chi_0^{-1}(T)/[d\chi_0^{-1}(T)/dT]$ exhibits a linear relationship with temperature, with slopes of $1/\beta$ and $1/\gamma$, respectively. As shown in Fig. 5(c), $\beta = 0.339(1)$ with $T_C = 178.021(1)$ K and $\gamma = 1.116(6)$ with $T_C = 178.134(1)$ K are obtained using the KF technique. The critical exponents obtained by the KF method closely match those extracted by the MAP iteration, confirming the reliability of the fitting results. Meanwhile, according to Eq. (5), δ can be determined by fitting the isotherm $M(H)$ at T_C. As shown in Fig. 5(d), it yields $\delta = 4.504(5)$. Although these critical exponents are obtained independently, they are inherently connected, as indicated by the Widom scaling law [56]:

$$\delta = 1 + \frac{\gamma}{\beta}. \tag{8}$$

Using the values obtained by the MAP iteration and KF methods, $\delta = 4.276(5)$ and $\delta = 4.292(1)$ are obtained by the Widom scaling law, respectively, confirming the reliability and self-consistency of the obtained critical exponents.

Figure 6(a) replots the final MAP with the obtained β and γ in the high-field region. In this region, all the straight lines are parallel to each other and the line at T_C crosses the origin. According to the universality principle of phase transitions, $M(H)$ curves near the critical temperature satisfy the scaling equation [52]:

$$M(H, \varepsilon) = \varepsilon^{\beta} f_{\pm}(H/\varepsilon^{\beta+\gamma}). \tag{9}$$

Here, f_+ for $T > T_C$ and f_- for $T < T_C$ are the regular functions. The rescaled $M(H)$ curves collapse onto two independent branches above and below T_C, respectively, as shown in Fig. 6(b). The scaling equation can also be expressed as [52]

$$\frac{M}{H^{1/\delta}} = h\left(\frac{\varepsilon}{H^{1/(\beta+\gamma)}}\right). \tag{10}$$

Here, h is the normalizing function. As seen in the inset of Fig. 6(b), the $M(H)$ curves around T_C scale onto a single universal curve, with T_C corresponding exactly to a zero transverse coordinate.

Table I lists the critical exponents of Cr_2Te_3 single crystals determined using various techniques, along with those of different theoretical models and related materials for comparison. The critical parameters of Cr_2Te_3 cannot be categorized into a single universality class, which is common in the Cr_xTe_y family due to the complex and multiple magnetic interactions. For instance, β of Cr_4Te_5 is close to the 3D-Heisenberg model while γ approaches the 3D-Ising and 3D-XY model [42]. For Cr_5Te_6, its critical exponents lie between the mean-field model and 3D-Heisenberg model [43]. For Cr_2Te_3, the critical exponent $\beta = 0.340(5)$

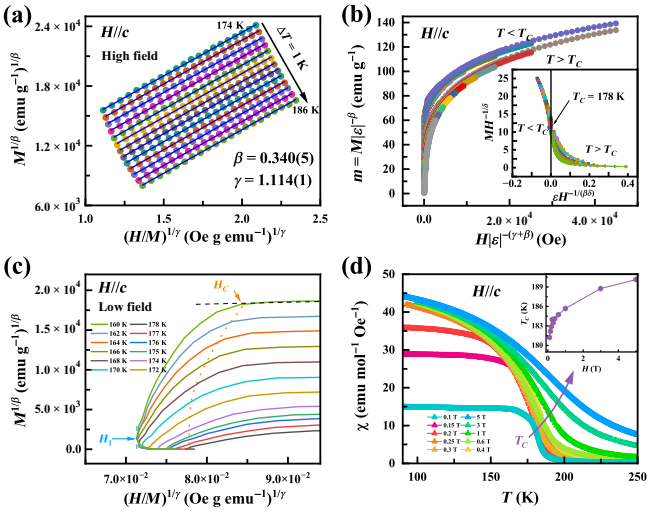

FIG. 6. (a) MAP with the obtained critical exponents in the high-field region for $H//c$. (b) Scaling plot of normalized $m(h)$ curves for $H//c$ (the insets show scaling plots of $MH^{-1/\delta}$ vs $\varepsilon H^{-1/(\beta\delta)}$). (c) MAP in the low-field region for $H//c$. (d) $\chi(T)$ under different fields.

TABLE I. Critical exponents of Cr_2Te_3 single crystal, different theoretical models, and related Cr-based compounds [MAP, modified Arrott plot; KF, Kouvel-Fisher (KF) technique; CI, critical isotherm analysis].

Composition	Reference	Technique	T_C (K)	β	γ	δ
Cr_2Te_3 ($H//c$)	This work	MAP	178.065(4)	0.340(5)	1.114(1)	4.276(5)
		KF	178.021(1)	0.339(1)	1.116(6)	4.292(1)
		CI				4.504(5)
Mean field		theory		0.5	1.0	3.0
3D-XY $\{d:n\}=\{3:2\}$		theory		0.345	1.316	4.81
3D-Heisenberg $\{d:n\}=\{3:3\}$		theory		0.365	1.386	4.8
3D-Ising $\{d:n\}=\{3:1\}$		theory		0.325	1.24	4.82
Tricritical mean field		theory		0.25	1.0	5.0
2D long range $\{d:n\}=\{2:1\}$		theory		0.298	1.393	5.67
2D short range $\{d:n\}=\{2:1\}$		theory		0.125	1.75	15.0
CrI_3 ($H//c$)	[51]	MAP	60.0	0.284(3)	1.146(1)	5.04(1)
$Cr_2Ge_2Te_6$ ($H//c$)	[50]	MEC	66.4	0.177(9)	1.746(8)	10.869(5)
$Cr_{0.62}Te$ ($H//c$)	[46]	MAP	230.76(9)	0.314(7)	1.83(2)	6.83(7)
Cr_3Te_4 ($H//c$)	[44]	KF	313.793(6)	0.369(7)	1.303(4)	4.525(1)
Cr_5Te_6 ($H//ab$)	[42]	MAP	338.170(1)	0.405(1)	1.200(1)	3.96(2)
Cr_4Te_5 ($H//ab$)	[43]	MAP	318.70(2)	0.388(4)	1.290(8)	4.32(3)

closely aligns with the 3D-XY model with $\{d:n\}=\{3:2\}$, where d represents the spatial dimensionality and n denotes the spin dimensionality. However, γ lies between the tricritical mean-field models and the 3D-Ising model with $\{d:n\}=\{3:1\}$. As shown in Table I, the critical exponent γ of Cr_2Te_3 bears resemblance to that of CrI_3.

Moreover, the critical exponents provide evidence supporting the existence of long-range magnetic order in 2D Cr_2Te_3 as previously discussed [34]. In the case of a homogeneous magnet, the universality of magnetic phase transitions is determined by the exchange distance of spin $J(r)$. According to renormalized group theory, there is $J(r)\approx r^{-(d+\sigma)}$ for the long-range interaction, while $J(r)\approx e^{-r/b}$ for the short-range interaction, where r denotes the distance, σ is a positive constant, and b is the spatial scaling factor [54,57,58]. The spin interaction related to σ is determined by [54,57,58]

$$\gamma = 1+\frac{4}{d}\frac{n+2}{n+8}\Delta\sigma+\frac{8(n+2)(n-4)}{d^2(n+8)^2}\times\left[1+\frac{2G(\frac{d}{2})(7n+20)}{(n-4)(n+8)}\right]\Delta\sigma^2, \quad (11)$$

where $\Delta\sigma=\sigma-(d/2)$, $G(d/2)=3-\frac{1}{4}(d/2)^2$. Based on the experimental value of $\gamma=1.114(1)$ and the 3D crystal structure, $\sigma=1.71(6)$ is calculated, which falls between the long-range and short-range interactions $(3/2<\sigma<2)$.

For a magnetic system with multiple phase transitions, the scaling curves usually diverge in the low-field region, as shown in Fig. 6(c). Two different turning points appear at H_1 and H_C, respectively. Based on the slope of the MAP, it can be determined that a second-order phase transition exists at H_C while a first-order one occurs at H_1. Figure 6(d) displays $\chi(T)$ under different external magnetic fields, the inset showing the field dependence of T_C. It is evident that T_C increases as the magnetic field increases. By combining the above transition points, the H-T phase diagram of Cr_2Te_3 can be derived, as shown in Fig. 7(a). The phase diagram is divided into four regions by three phase-transition boundaries, which are, respectively, labeled as PM (paramagnetic state), FFM (forced ferromagnetic phase), canted FM1, and canted FM2 representing two kinds of canted spin textures.

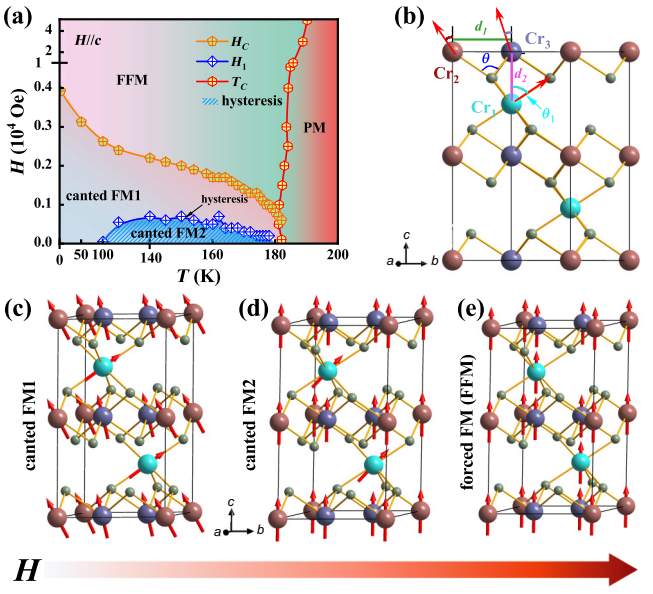

FIG. 7. (a) H-T phase diagram of Cr_2Te_3 single crystal for $H//c$. (b) Magnetic interactions between different positions of Cr ions. (c)–(e) Magnetic structures for canted FM1, canted FM2, and forced FM (FFM).

The multiple phases and transitions in Cr_2Te_3 are a result of the various magnetic couplings caused by its unique crystal structure. Figure 7(b) provides a schematic representation of the exchange couplings, showing the different positions of the Cr atoms: Cr1, Cr2, and Cr3. Cr1 ions are located in the vacancy layers, while Cr2 and Cr3 ions are classified based on the number of nearest neighbors along the c axis. Cr2 has no nearest neighbor, while Cr3 has one. Previous studies indicate that the spin-canting model arises from the competition between interlayered direct interaction and intralayered superexchange, which depend on the atomic spaces [35,59]. The superexchange is associated with the angle of Cr-Te-Cr [35,59]. In Fig. 7(b), the distances between different Cr atoms are $d_1 = 3.9337$ Å, $d_2 = 3.0182$ Å, and $\theta = 92.96^\circ$, which indicate that the FM coupling dominates in the intralayers while the AFM coupling prevails between the interlayers. Density functional theory (DFT) suggests that the spins can align only in parallel when the average moments of Cr are $3.03\mu_B$/Cr, which is notably higher than the experimental value. This implies that the spins should be canted to counterbalance a portion of the magnetic moments [36,37]. Between Cr1 and Cr3, the spins are deflected in different directions due to the direct AFM exchange, resulting in polar angles indicated in blue and purple, respectively. Due to the predominance of intralayered FM coupling, Cr2 and Cr3 have similar spin-canting directions. However, since Cr2 has no nearest neighbor along the c axis compared to Cr3, the polar angle of Cr2 is larger. On the other hand, the spin-canting angle for Cr2 and Cr3 are smaller than that of Cr1 (θ_1). As shown in Fig. 7(c), the ground magnetic state of Cr_2Te_3 actually is a ferrimagnetic (FIM) configuration when projected to the in plane, which is consistent with the decline of $\chi(T)$ curves. As the field increases, the Cr spins canted in the fully occupied layers (i.e., Cr2 and Cr3) are preferred to be polarized, resulting in another canted or noncollinear model, as shown in Fig. 7(d). With a further increase of the field, the polar angle is completely polarized into the FFM state. On the other hand, with the increase of temperature, the canted FM or FFM states transform to the PM phase above approximately 181 K. The thermal hysteresis in $\chi(T)$ curves indicates that the transition to canted FM2 under lower field is of the first-order type, while the transition from canted FM1 or FFM to PM under higher field is of the second-order one. This means that the first-order magnetic transition under low field can be suppressed by the external magnetic field.

IV. CONCLUSION

In summary, the magnetization and magnetic anisotropy of Cr_2Te_3 single crystal were systematically investigated. FM-PM transitions were observed for both $H//c$ and $H//ab$ at $T_C \sim 181$ K. Additional, the study of magnetization revealed exotic magnetic behaviors, such as a field-modulated first-order transition, a canted FM coupling rather than spin-glass behaviors as previous reported. Anisotropic magnetization showed significant PMA with a negligible saturation field for $H//c$ but a distinct one up to 155 kOe for $H//ab$, stronger than any other Cr-based TMDCs. Critical exponents $\beta = 0.340(5)$, $\gamma = 1.114(1)$, and $\delta = 4.504(5)$ were obtained for $H//c$, which do not belong to any university classic model but fall between the 3D-XY and 3D-Ising models, suggesting strong anisotropic magnetic coupling. An H-T phase diagram for Cr_2Te_3 single crystal was constructed for $H//c$, revealing the canted FM1, canted FM2, FFM, and PM phases. The phase diagram showed that the transition to the canted FM2 under lower field is of the first-order type, but can be suppressed into a second-order one by the external magnetic field. The multiple phase transitions and complex magnetic structures in Cr_2Te_3 arise from the competition between the intralayered superexchange (FM couplings) and the interlayered direct interactions (AFM coupling). The various magnetic configurations and PMA of Cr_2Te_3 make it highly potential for spintronic device applications.

ACKNOWLEDGMENTS

This work was supported by the National Natural Science Foundation of China (Grants No. 12374128, No. 12074386, No. 11874358, No. 11974181, No. 12204006, and No. 12250410238), the Alliance of International Science Organizations (Grant No. ANSO-VF-2022-03). A proportion of this work was supported by the High Magnetic Field Laboratory of Anhui Province. This work is supported by Basic Research Program of the Chinese Academy of Sciences Based on Major Scientific Infrastructures Grant No. JZHKYPT-2021-08.

[1] G. Cheng, L. Li, Z. Li, H. Ji, A. Stern, Y. Xia, T. Cao, W. Bao, C. Wang, Y. Wang *et al.*, Discovery of intrinsic ferromagnetism in two-dimensional van der Waals crystals, Nature (London) **546**, 265 (2017).

[2] B. Huang, G. Clark, E. Navarro-Moratalla, D. R. Klein, R. Cheng, K. L. Seyler, D. Zhong, E. Schmidgall, M. A. McGuire, D. H. Cobden *et al.*, Layer-dependent ferromagnetism in a van der Waals crystal down to the monolayer limit, Nature (London) **546**, 270 (2017).

[3] L. Zhang, J. Zhou, H. Li, L. Shen, and Y. Feng, Recent progress and challenges in magnetic tunnel junctions with 2D materials for spintronic applications, Appl. Phys. Rev. **8**, 021308 (2021).

[4] Y. Feng, L. Shen, M. Yang, A. Wang, M. Zeng, Q. Wu, S. Chintalapati, and C. Chang, Prospects of spintronics based on 2D materials, Wiley Interdiscip. Rev.: Comput. Mol. Sci. **7**, e1313 (2017).

[5] X. Zhang, W. Liu, W. Niu, Q. Lu, W. Wang, A. Sarikhani, X. Wu, C. Zhu, J. Sun, M. Vaninger *et al.*, Self-intercalation tunable interlayer exchange coupling in a synthetic van der

Waals antiferromagnet, Adv. Funct. Mater. **32**, 2202977 (2022).

[6] B. Tang, X. Wang, M. Han, X. Xu, Z. Zhang, C. Zhu, X. Cao, Y. Yang, Q. Fu, J. Yang *et al.*, Phase engineering of Cr_5Te_8 with colossal anomalous Hall effect, Nat. Electron. **5**, 224 (2022).

[7] D. Zhao, L. Zhang, I. A. Malik, M. liao, W. Cui, X. Cai, C. Zheng, L. Li, X. Hu, D. Zhang *et al.*, Observation of unconventional anomalous Hall effect in epitaxial CrTe thin films, Nano Res. **11**, 3116 (2018).

[8] R. Saha, H. L. Meyerheim, B. Göbel, B. K. Hazra, H. Deniz, K. Mohseni, V. Antonov, A. Ernst, D. Knyazev, A. edoya Pinto *et al.*, Observation of Néel-type skyrmions in acentric self-intercalated $Cr_{1+\delta}Te_2$, Nat. Commun. **13**, 3965 (2022).

[9] Y. Wang, J. Yan, J. Li, S. Wang, M. Song, J. Song, Z. Li, K. Chen, Y. Qin, L. Ling *et al.*, Magnetic anisotropy and topological Hall effect in the trigonal chromium tellurides Cr_5Te_8, Phys. Rev. B **100**, 024434 (2019).

[10] Y. Chen, Y. Zhu, R. Lin, W. Niu, R. Liu, W. Zhuang, X. Zhang, J. Liang, W. Sun, Z. Chen *et al.*, Observation of colossal topological Hall effect in noncoplanar ferromagnet Cr_5Te_6 thin films, Adv. Funct. Mater. **33**, 2302984 (2023).

[11] B. Li, X. Deng, W. Shu, X. Cheng, Q. Qian, Z. Wan, B. Zhao, X. Shen, R. Wu, S. Shi *et al.*, Air-stable ultrathin Cr_3Te_4 nanosheets with thickness-dependent magnetic biskyrmions, Mater. Today **57**, 66 (2022).

[12] Y. Wang, S. Kajihara, H. Matsuoka, B. K. Saika, K. Yamagami, Y. Takeda, H. Wadati, K. Ishizaka, Y. Iwasa, and M. Nakano, Layer-number-independent two-dimensional ferromagnetism in Cr_3Te_4, Nano Lett. **22**, 9964 (2022).

[13] R. Chua, J. Zhou, X. Yu, W. Yu, J. Gou, R. Zhu, L. Zhang, M. Liu, M. B. Breese, W. Chen *et al.*, Room temperature ferromagnetism of monolayer chromium telluride with perpendicular magnetic anisotropy, Adv. Mater. **33**, 2103360 (2021).

[14] J. Xian, C. Wang, J. Nie, R. Li, M. Han, J. Lin, W. Zhang, Z. Liu, Z. Zhang, M. Miao *et al.*, Spin mapping of intralayer antiferromagnetism and field-induced spin reorientation in monolayer $CrTe_2$, Nat. Commun. **13**, 257 (2022).

[15] X. Zhang, Q. Lu, W. Liu, W. Niu, J. Sun, J. Cook, M. Vaninger, P. F. Miceli, D. J. Singh, S.-W. Lian *et al.*, Room-temperature intrinsic ferromagnetism in epitaxial $CrTe_2$ ultrathin films, Nat. Commun. **12**, 2492 (2021).

[16] M. A. McGuire, V. O. Garlea, S. KC, V. R. Cooper, J. Yan, H. Cao, and B. C. Sales, Antiferromagnetism in the van der Waals layered spin-lozenge semiconductor $CrTe_3$, Phys. Rev. B **95**, 144421 (2017).

[17] M. Wang, L. Kang, J. Su, L. Zhang, H. Dai, H. Cheng, X. Han, T. Zhai, Z. Liu, and J. Han, Two-dimensional ferromagnetism in CrTe flakes down to atomically thin layers, Nanoscale **12**, 16427 (2020).

[18] Y. Wen, Z. Liu, Y. Zhang, C. Xia, B. Zhai, X. Zhang, G. Zhai, C. Shen, P. He, R. Cheng *et al.*, Tunable room-temperature ferromagnetism in two-dimensional Cr_2Te_3, Nano Lett. **20**, 3130 (2020).

[19] C. Chen, X. Chen, C. Wu, X. Wang, Y. Ping, X. Wei, X. Zhou, J. Lu, L. Zhu, J. Zhou *et al.*, Air-stable 2D Cr_5Te_8 nanosheets with thickness-tunable ferromagnetism, Adv. Mater. **34**, 2107512 (2022).

[20] V. Kanchana, G. Vaitheeswaran, and M. Rajagopalan, Pressure-induced structural and magnetic phase transition in ferromagnetic CrTe, J. Magn. Magn. Mater. **250**, 353 (2002).

[21] C. Li, K. Liu, C. Jin, D. Jiang, Z. Jiang, T. Wen, B. Yue, and Y. Wang, Pressure-induced structural phase transition, anomalous insulator-to-metal transition, and n–p conduction-type switching in defective, NiAs-type $Cr_{1-\delta}Te$, Inorg. Chem. **61**, 11923 (2002).

[22] L. Wu, L. Zhou, X. Zhou, C. Wang, and W. Ji, In-plane epitaxy-strain-tuning intralayer and interlayer magnetic coupling in $CrSe_2$ and $CrTe_2$ monolayers and bilayers, Phys. Rev. B **106**, L081401 (2022).

[23] Y. Zhong, C. Peng, H. Huang, D. Guan, J. Hwang, H. H. Kuan, Y. Hu, C. Jia, B. Moritz, D. Lu *et al.*, From Stoner to local moment magnetism in atomically thin Cr_2Te_3, Nat. Commun. **14**, 5340 (2023).

[24] J. Yao, H. Wang, B. Yuan, Z. Hu, C. Wu, and A. Zhao, Ultrathin van der Waals antiferromagnet $CrTe_3$ for fabrication of in-plane $CrTe_3/CrTe_2$ monolayer magnetic heterostructures, Adv. Mater. **34**, 2200236 (2022).

[25] J. H. Jeon, H. R. Na, H. Kim, S. Lee, S. Song, J. Kim, S. Park, J. Kim, H. Noh, G. Kim *et al.*, Emergent topological Hall effect from exchange coupling in ferromagnetic Cr_2Te_3/noncoplanar antiferromagnetic Cr_2Se_3 bilayers, ACS Nano **16**, 8974 (2022).

[26] J. Chen, L. Wang, M. Zhang, L. Zhou, R. Zhang, L. Jin, X. Wang, H. Qin, Y. Qiu, J. Mei *et al.*, Evidence for magnetic skyrmions at the interface of ferromagnet/topological-insulator heterostructures, Nano Lett. **19**, 6144 (2019).

[27] L. Zhou, J. Chen, X. Chen, B. Xi, Y. Qiu, J. Zhang, L. Wang, R. Zhang, B. Ye, P. Chen *et al.*, Topological Hall effect in traditional ferromagnet embedded with black-phosphorus-like bismuth nanosheets, ACS Appl. Mater. Inter. **12**, 25135 (2020).

[28] R. Anupam, G. Samaresh, D. Rik, T. Pramanik, H. Cheng-Chih, R. Amritesh, and S. K. Banerjee, Perpendicular magnetic anisotropy and spin glass-like behavior in molecular beam epitaxy grown chromium telluride thin films, ACS Nano **9**, 3772 (2015).

[29] H. Yang, F. Wang, H. Zhang, L. Guo, L. Hu, L. Wang, D. J. Xue, and X. Xu, Solution synthesis of layered van der Waals (vdW) ferromagnetic $CrGeTe_3$ nanosheets from a non-vdW Cr_2Te_3 template, J. Am. Chem. Soc **142**, 4438 (2020).

[30] H. Chi, Y. Ou, T. B. Eldred, W. Gao, S. Kwon, J. Murray, M. Dreyer, R. E. Butera, A. C. Foucher, H. Ambaye *et al.*, Strain-tunable Berry curvature in quasi-two-dimensional chromium telluride, Nat. Commun. **14**, 3222 (2023).

[31] T. Hashimoto, K. Hoya, M. Yamaguchi, and I. Ichitsubo, Magnetic properties of single crystals $Cr_{2-\delta}Te_3$, J. Phys. Soc. Jpn. **31**, 679 (1971).

[32] J. Dijkstra, H. H. Weitering, C. F. van Bruggen, C. Haas, and R. A. de Groot, Band-structure calculations, and magnetic and transport properties of ferromagnetic chromium tellurides (CrTe, Cr_3Te_4, Cr_2Te_3), J. Phys.: Condens. Matter **1**, 9141 (1989).

[33] S. J. Youn, S. K. Kwon, and B. I. Min, Correlation effect and magnetic moments in Cr_2Te_3, J. Appl. Phys. **101**, 09G522 (2007).
[34] A. L. Coughlin, D. Xie, Y. Yao, X. Zhan, Q. Chen, H. Hewa-Walpitage, X. Zhang, H. Guo, H. Zhou, J. Lou *et al.*, Near degeneracy of magnetic phases in two-dimensional chromium telluride with enhanced perpendicular magnetic anisotropy, ACS Nano **14**, 15256 (2020).
[35] Z. Jiang, X. Liang, X. Luo, J. J. Gao, W. Wang, T. Y. Wang, X. C. Yang, X. L. Wang, L. Zhang, Y. Sun *et al.*, Evolution of ground state in Cr_2Te_3 single crystal under applied magnetic field, Phys. Rev. B **106**, 094407 (2022).
[36] J. Yang, C. Zhu, Y. Deng, B. Tang, and Z. Liu, Magnetism of two-dimensional chromium tellurides, iScience **26**, 106567 (2023).
[37] M. Bian, A. N. Kamenskii, M. Han, W. Li, S. Wei, X. Tian, D. B. Eason, F. Sun, K. He, H. Hui *et al.*, Magnetism of two-dimensional chromium tellurides, Mater. Res. Lett. **9**, 205 (2021).
[38] T. Hamasaki, T. Hashimoto, Y. Yamaguchi, and H. Watanabe, Neutron diffraction study of Cr_2Te_3 single crystal, Solid State Commun. **16**, 895 (1975).
[39] A. F. Andresen, The magnetic structure of Cr_2Te_3, Cr_3Te_4, and Cr_5Te_6, Acta Chem. Scand. **24**, 3495 (1970).
[40] H. Li, L. Wang, J. Chen, T. Yu, L. Zhou, Y. Qiu, H. He, F. Ye, I. K. Sou, and G. Wang, Molecular beam epitaxy grown Cr_2Te_3 thin films with tunable Curie temperatures for spintronic devices, ACS Appl. Nano Mater. **2**, 6809 (2019).
[41] S. Blundell, *Magnetism in Condensed Matter* (Science Press, Beijing, 2001), p. 48.
[42] L. Zhang, Q. Xiao, F. Chen, Z. Feng, S. Cao, J. Zhang, and J.-Y. Ge, Multiple magnetic phase transitions and critical behavior in single crystal Cr_5Te_6, J. Magn. Magn. Mater. **546**, 168770 (2022).
[43] L. Z. Zhang, A. L. Zhang, X. D. He, X. W. Ben, Q. L. Xiao, W. L. Lu, F. Chen, Z. Feng, S. Cao, J. Zhang *et al.*, Critical behavior and magnetocaloric effect of the quasi-two-dimensional room-temperature ferromagnet Cr_4Te_5, Phys. Rev. B **101**, 214413 (2020).
[44] A. Wang, A. Rahman, Z. Du, J. Zhao, F. Meng, W. Liu, J. Fan, C. Ma, M. Ge, l. Pi *et al.*, Field-dependent anisotropic room-temperature ferromagnetism in Cr_3Te_4, Phys. Rev. B **108**, 094429 (2023).
[45] J. Liu, B. Ding, J. Liang, X. Li, Y. Yao, and W. Wang, Magnetic skyrmionic bubbles at room temperature and sign reversal of the topological Hall effect in a layered ferromagnet $Cr_{0.87}Te$, ACS Nano **16**, 13911 (2022).
[46] Y. Liu and C. Petrovic, Critical behavior of the quasi-two-dimensional weak itinerant ferromagnet trigonal chromium telluride $Cr_{0.62}Te$, Phys. Rev. B **96**, 134410 (2017).
[47] C. A. M. Mulder, A. J. van Duyneveldt, and J. A. Mydosh, Susceptibility of the CuMn spin-glass: Frequency and field dependences, Phys. Rev. B **23**, 1384 (1981).
[48] L. Meng, J. Xiang, Z. Mi, H. Zhao, Z. Wang, E. Liu, G. Chen, Z. Ren, G. Li, and P. Sun, Nonsaturating magnetoresistance, anomalous Hall effect, and magnetic quantum oscillations in the ferromagnetic semimetal PrAlSi, Phys. Rev. B **102**, 085143 (2020).
[49] Y. Liu and C. Petrovic, Anisotropic magnetic entropy change in $Cr_2X_2Te_6$ (X = Si and Ge), Phys. Rev. Mater. **3**, 014001 (2019).
[50] W. Liu, Y. Dai, Y.-E. Yang, J. Fan, L. Pi, L. Zhang, and Y. Zhang, Critical behavior of the single-crystalline van der Waals bonded ferromagnet $Cr_2Ge_2Te_6$, Phys. Rev. B **98**, 214420 (2018).
[51] Y. Liu and C. Petrovic, Three-dimensional magnetic critical behavior in CrI_3, Phys. Rev. B **97**, 014420 (2018).
[52] L. Zhang, Critical behaviors of helimagnetic ordering systems relating to skyrmion, Acta. Phys. Sin. **67**, 137501 (2018).
[53] A. Arrott, Criterion for ferromagnetism from observations of magnetic isotherms, Phys. Rev. **108**, 1394 (1957).
[54] M. E. Fisher, The theory of equilibrium critical phenomena, Rep. Prog. Phys. **30**, 615 (1967).
[55] J. S. Kouvel and M. E. Fisher, Detailed magnetic behavior of nickel near its Curie point, Phys. Rev. **136**, A1626 (1964).
[56] B. Widom, Equation of state in the neighborhood of the critical point, J. Chem. Phys. **43**, 3898 (1965).
[57] M. E. Fisher, S.-k. Ma, and B. Nickel, Critical exponents for long-range interactions, Phys. Rev. Lett. **29**, 917 (1972).
[58] H. Liu, J. Fan, H. Zheng, J. Wang, C. Ma, H. Wang, L. Zhang, C. Wang, Y. Zhu, and H. Yang, Magnetic properties and critical behavior of quasi-2D layered Cr_4Te_5 thin film, Front. Phys. **18**, 13302 (2023).
[59] Q. Liu, Y. Wang, Y. Zhao, Y. Guo, X. Jiang, and J. Zhao, Composition-dependent magnetic ordering in freestanding 2D non-van der Waals $Cr_2Te_xSe_{3-x}$ Crystals, Adv. Funct. Mater. **32**, 2113126 (2022).